UPDATE ON THE ATTITUDE STATE AND MOTION OF SPACE DEBRIS FROM GROUND-BASED OBSERVATIONS AT THE SWISSOGS

Julian Rodriguez-Villamizar[(1)], Alessandro Vananti[(1)], Thomas Schildknecht[(1)], Danica Žilková[(2)], and Jiří Šilha[(2)]

[(1)]*Astronomical Institute, University of Bern, Switzerland, julian.rodriguez@unibe.ch*
[(2)]*Comenius University, Faculty of Mathematics, Physics and Informatics, Bratislava, Slovakia*

ABSTRACT

The unprecedented growing number of human-made objects in the near-Earth space environment calls for immediate action. Current initiatives propose the direct removal of selected targets or the so-called on-orbit servicing aiming to extend the life cycle of selected missions. For the design of such missions, the understanding of the attitude and the attitude motion of the target object becomes imperative. Ground-based observations may help providing evidence about the tumbling state of observable targets employing different observation techniques.
The Swiss Optical Ground Station and Geodynamics Observatory (SwissOGS) Zimmerwald, located near Bern, Switzerland, and operated by the Astronomical Institute of the University of Bern, provides measurements to maintain a database containing the synodic period of diverse resident space objects being estimated from the observed lightcurve. The measurements may be acquired using CCD or sCMOS detectors mounted on different telescopes with the possibility to include spectral filters in specific standard photometric systems. In addition, available laser ranging measurements to uncontrolled targets carrying retroreflectors may serve as an independent technique to validate and complement results obtained using optical-passive systems.
In this work, we will focus on observations gathered for specific targets that were main subject in previous scientific studies, such as Envisat, Topex/Poseidon, Jason-2 and ERS-2, from which we were able to collect measurements and infer information about its attitude and attitude motion. We highlight the acquisition of daylight lightcurves for Envisat, the simultaneous acquisition of passive and active optical measurements for Topex/Poseidon and ERS-2, the most recent light curves extracted using the newly systems available at the SwissOGS, which consist of a sCMOS detector and the Shelyak LISA spectrograph mounted on the Zimmerwald Multiple Applications Instrument (ZimMAIN) telescope.

Keywords: Satellite Laser Ranging, Passive Optical, Attitude States, Space Debris.

1. INTRODUCTION

The European Space Agency (ESA) Zero Debris Approach is an initiative towards a sustainable use of the outer space. The Zero Debris Approach entails a more sustainable strategy for space operations and the End of Life phase of existing missions, boosting the disposal success rate from the protected regions, and encouraging removal actions [1]. For the successful implementation of the envisioned strategy, the detection, tracking and characterization of the space debris population is of paramount importance. In that context, through a network of ground- and space-based sensors, we can infer information about (non-exhaustive list):

- **Orbits.** Available measurements will permit us to determine and improve the orbits of the observable space debris (SD). Orbits are fundamental to predict where the SD will be in the future, or even in the past if we consider parenting of fragments after break up events, and the assessment of close conjunction event, among others.
- **Tumbling rates, target object shape and physical properties.** Information in the form of lightcurves (LC): changes in brightness over time using electro-optical systems; laser ranges residuals: actual topocentric measured ranges minus predicted ones; and radar cross-sections: changes in the received signal strength over time using radio signals may provide evidence of the attitude state and its evolution over time of the SD.

This information is a valuable asset to our understanding of the SD population, and evolution over time. On a technical note, it is crucial to define the requirements on new missions for the End of Life phase, or for missions aiming at an active removal of SD. One example highlighting the relevance of such data is the onboard inclusion, or exclusion, of passivation mechanisms. Upper stage rocket bodies with a tumbling rate of 0.7 rad/sec, showed that active debris removal missions, based on captured nets, could be jeopardized [2]. If we compare the values used in the simulations by [2], with archive historical values obtained at the SwissOGS [3], we see that there are

many objects that might pose a challenge: the so-called fast rotators with synodic periods between 100 to 1 seconds. In addition, due to the external perturbations acting on the SD, we need frequent updates accounting for all possible changes in the attitude state of the SD to be removed. This paper provides examples showing the results obtained from measurements acquired at the SwissOGS.

2. INSTRUMENTATION

The measurements that we present in this work were acquired with different systems. We used the Zimmerwald Laser and Astrometric Telescope and the Zimmerwald Multiple Applications Instrument telescope, which we refer here onward as ZIMLAT and ZimMAIN, respectively (Figure 1). Both telescopes are alt-azimuth Ritchey-Chrétien. ZIMLAT has a 1 m aperture, *f*/4, and a total angular slew rate of 30 °/sec, while ZimMAIN has a 0.8 m aperture, *f*/8, and a total angular slew rate of 13°/sec. The passive optical detectors include the CCD Spectral Instruments 1100 (SI1100), the sCMOS Andor Neo 5.5, and the Shelyak LISA spectrograph, all commercially available off-the-shelf. The laser ranging system has a nominal power of 1 W at 532 nm, with a repetition rate of 100 Hz. The Andor Neo 5.5 camera was installed on ZimMAIN at the beginning of 2022, since ZIMLAT went out of operations due to the replacement of the dome. The pixel scale of the Andor Neo 5.5 yields 0.173 and 0.242 arcseconds/pixel in ZIMLAT and ZimMAIN, respectively.

Figure 1. ZIMLAT (left) and ZimMAIN (right) at the SwissOGS operated by the Astronomical Institute of the University of Bern.

3. ENVISAT

In this section, we follow-up on the work presented in [4]. Note that from Figure 2, the LCs a) and b), were already published, however, we add them here to further correlate distinctive features with the new observations. The depicted LCs in Figure 2 were observed on: a) April 15, 2021, b) April 24, 2021, c) May 9, 2021, and d) January 1, 2022. All of them were acquired with ZIMLAT using the Andor Neo 5.5 camera during daylight. Further information is provided by the relative geometry between the SwissOGS and Envisat at the different observation epochs (see Figure 3) to highlight the relevance of having observations with different aspect angles and illumination conditions.

In addition to the passive optical measurements, we were able to collect laser ranges on April 15, 2021, and on May 9, 2021. After inspection of the retrieved data, the length of the observed data did not allow to recover information about the synodic period of the object.

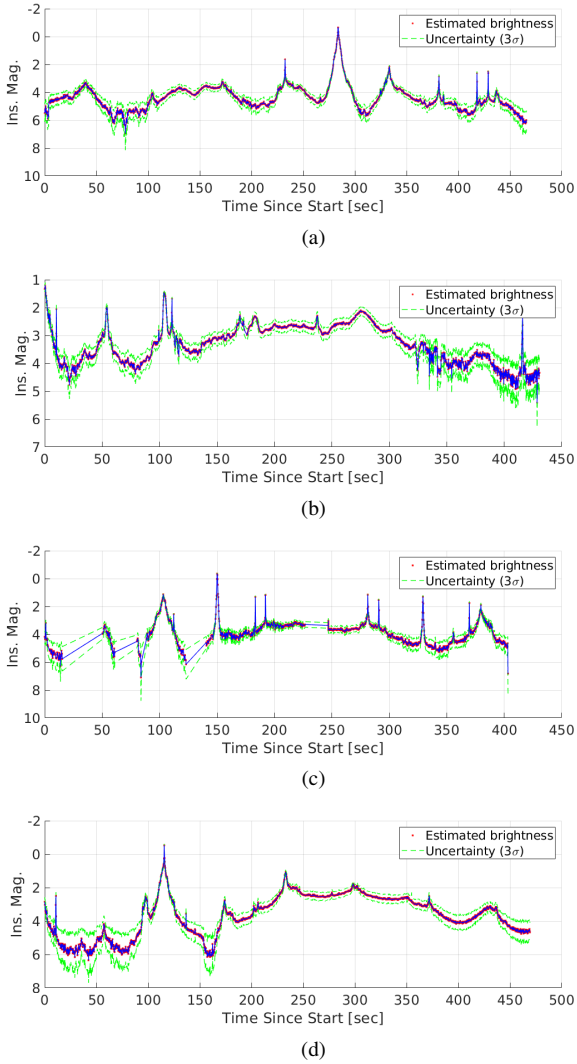

Figure 2. Post-processed LCs acquired during daylight with ZIMLAT on the following dates: a) April 15, 2021, b) April 24, 2021, c) May 9, 2021, and d) January 1, 2022.

3.1. Relative Geometry

All observations correspond to high-culmination passes, which are of particular interest, since we can cover a larger orbital arc (see Figure 3). To remove the impact of the relative geometry between the Sun, the target and the station, extinction effects and others, we detrended the raw LCs using a third degree polynomial, prior to the estimation of the synodic periods. We tested the detrending normalizing the estimated brightness with the respec-

tive airmass, or assuming a specular sphere phase function [7]. For the tested cases, the main trend showed no significant variation using either the airmass or the specular sphere phase angles. In addition, the detrending of the LCs in Figure 2, corresponded only to a shift in brightness for the LCs a), b), and c). The detrending of the LC d), however, enhanced the features depicted within the seconds 150 and 400.

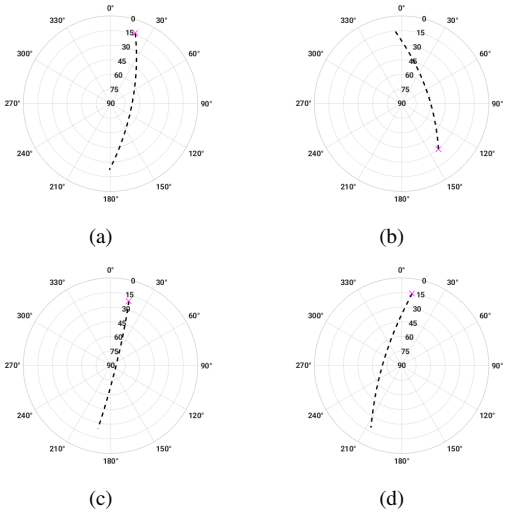

Figure 3. Relative geometry between the SwissOGS and different passes of Envisat corresponding to observations acquired on the following dates: a) April 15, 2021, b) April 24, 2021, c) May 9, 2021, and d) January 1, 2022. The magenta cross indicates the beginning of the pass to infer the flight direction.

3.2. Feature Identification

The first feature that draws attention is the peak on Figure 2 LC a) at about 280 seconds.The maximum has a difference in brightness of almost 5 magnitudes with respect to the average from the complete pass, and has a symmetric broad shape, i.e., it does not seem to correspond to a sudden glint. Dominant peaks in brightness with respect to the average are found at 0 seconds in the LC b) and at 125 seconds in the LC d). Main peaks in brightness, are surrounded by other consecutive prominent peaks, but with a difference of about 2 magnitudes with respect to the average. In addition, there are two peaks, with narrow shapes suggesting possible glints that are recognizable in the LCs a) and c). Moreover, in the LC c), the peaks repeat within the same LC.

3.3. New LCs with a sCMOS detector on ZimMAIN

Complementary to the LCs shown in Figure 2, in Figure 4 we show two examples of LCs acquired with the Andor Neo 5.5 camera mounted on the second focal station available in ZimMAIN. Both a) LCs in Figures 2

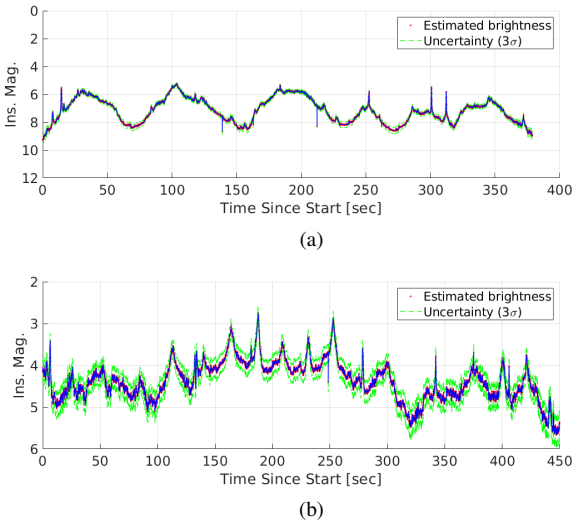

Figure 4. LCs acquired with the Andor Neo 5.5 camera on ZimMAIN: a) on September 12, 2022, and b) on November 2, 2022.

and 4 correlate with the three main peaks at seconds 40, 100 and 175 seconds, plus and two consecutive glints after 300 seconds in plot a), Figure 4. Nevertheless, the shape of the peaks that we see in Figure 4 a) have a more rounded shape and less difference in brightness than Figure 2. The LC b) in Figure 4 shows a possible symmetry in the right and left directions from second 225, but as of now, we cannot identify features correlating with the previous LCs.

Table 1. Estimated synodic period from the LCs in Figures 2 and 4.

Date	Period	1-sigma
15-04-2021	230.5	0.1
24-04-2021	226.7	0.5
09-05-2021	259.8	3.0
01-01-2022	242.0	2.0
12-09-2022	238.0	2.0
02-11-2022	256.3	2.0

3.4. Estimated Synodic Period

From the LCs shown in Figure 2 and 4, we estimated the synodic period of Envisat using the Phase Dispersion Minimization (PDM) method. The decision to use this method came from the fact that other methods available, such as Lomb-Scargle, failed in some cases; with the PDM method, we were able to estimate a period consistently for all passes. In Table 1, we show all estimated periods from the LCs in Figure 2 and 4. The estimated

periods do not show a definite clear trend that could be used to construct physical hypotheses. Moreover, the order of magnitude from the uncertainties associated to the estimated periods do not reflect this fact. For example consider the period of 259.8 seconds, which differs significantly from the previous periods about 30 seconds, while its uncertainty suggests that the estimated period is precise – about two orders of magnitude smaller than the actual value of the estimated period. To further improve our current information regarding the tumbling rate of Envisat, it would be ideal to track the defunct satellite with more than one station in Europe during the same orbital revolution. By doing that, we expect to recover the period more reliably.

4. TOPEX/POSEIDON

In this section, we present the results of a specific campaign. In the night of the 8th of May, 2021, we were able to observe 3 passes of the target object TOPEX/Poseidon with the Andor Neo 5.5 on ZIMLAT, and retrieve simultaneously laser ranges for two of the passes. The aim of the campaign is twofold. On the one hand, we wanted to analyze the impact of having information with different geometry, but within the same observation night. On the other hand, we wanted to see if we have consistent results using two independent techniques with the possibility of fusing the data in a subsequent step. For all LCs the detrending of the raw data was crucial for the following analysis.

4.1. Feature-Based Synodic Period Estimation

After a careful analysis of the three passes, we noticed that certain periodic patterns had different shapes within the same pass, and within the same campaign. Examples showing the different distinctive features that we found are shown in Figure 5. In Figure 5 a) we see different patterns within the first pass. In Figure 5 b), we see different patterns during the second pass. For both passes, the beginning of the passes show more variability than the end. One possible explanation might be the effect of the observation conditions: even if we are removing the main trend of the raw LC, the impact of the observation geometry, illumination conditions and aspect angle affect local features which cannot be removed without losing valuable information. To account for this variability, we developed and implemented the so-called *feature-based synodic period estimation* method. The method is described in the following steps:

(i) **Preprocessing of the raw LCs.** In this step, we check the acquired LCs, remove potential outliers and remove the main trend using polynomials.

(ii) **Pattern recognition of the different periodic patterns.** Each acquired LC is scanned for potential patterns using the PDM method (examples of such patterns are shown in Figure 5). Once the scanning of the LC is finished, a threshold is found from the construction of a loss function, which takes as arguments the standard deviation of the reconstructed phase, and the number of times that the pattern was found. After this threshold is applied, we construct *masters* of the different patterns.

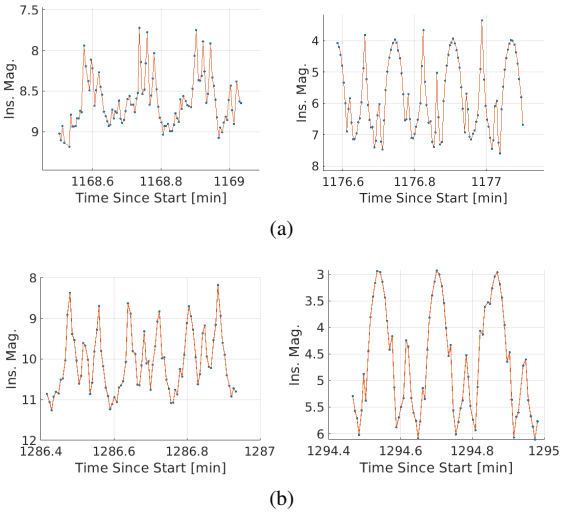

Figure 5. Details of observations from different LCs observed within the same observation night using the camera Andor Neo 5.5 on ZIMLAT during an observation campaign conducted on May 8, 2021.

(iii) **Split LCs according to the different patterns.** Afterwards, all available LCs are split according to the found patterns. Then, per each pattern the period is estimated using the pre-selected method, e.g., PDM, Lomb-Scargle, or any other available.

(iv) **Combine the estimated periods from the different patterns.** The last step of the method combines the different periods corresponding to the different features from the LCs using the maximum likelihood estimator taking into account the formal-errors per each period estimated from each available pattern. To do so, we assume that all the estimated periods per each pattern are samples from the normal distribution of the *true* period with their respective standard deviation.

An example of the estimated synodic period for one particular feature (see right plot in a), Figure 5) is shown in the left plot in Figure 6. Furthermore, the algorithm includes the possibility to smooth the selected pattern using a robust Box filter (see right plot in Figure 6).

4.2. Data Fusion

The method described in the previous section permits us to extend the analysis treating laser ranges residuals as another pattern. Note that a feature scaling

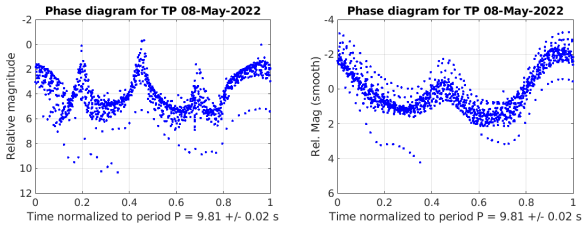

Figure 6. Phase diagrams with and without smoothing corresponding to a unique identified pattern (see right plot a) in Figure 5).

step to homogenize the measurements from the different observation techniques becomes mandatory. In Figure 7, we show the raw measurements (a) left), the post-processed raw measurements (a) right), the reconstructed periodogram using the Lomb-Scargle method (b) left), and the reconstructed phase diagram (b) right) for one of the passes that we observed simultaneously with passive optical.

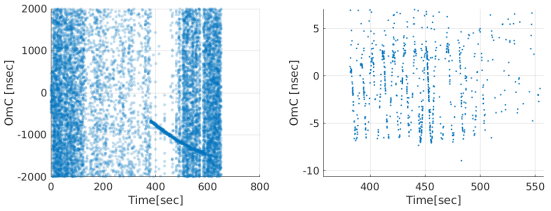

(a)

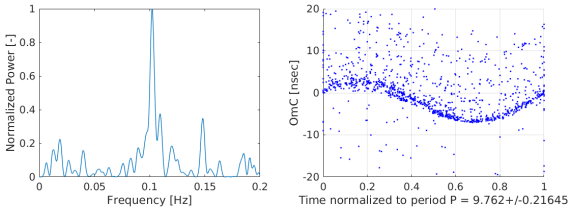

(b)

Figure 7. a) Details of the raw laser ranging residuals (left), and postprocessed signal (right). b) Periodogram (left) and reconstructed phase diagram (right). The pass was observed simultaneously with the Andor Neo 5.5 on ZIMLAT on May 8, 2021.

From Figure 7, we may draw the following conclusions. The predictions available were inaccurate, enforcing the use of large range gates, which ultimately increased significantly the noise level. Nevertheless, even with the relatively short portion of the pass with clear signal, we were able to see the periodic pattern of the retroreflector onboard of the defunct satellite and estimate its period with acceptable precision – one order of magnitude less than the value of the estimated period. Furthermore, by comparing the estimated period with the one obtained from passive optical measurements, we see that both are in agreement.

After the end of this campaign, we wanted to address the fact of having better orbit predictions, and its impact on the estimation of the synodic period. In Figure 8, we see how better predictions permit setting smaller range gates, which depicts the highly concentrated returns centred around zero. Additionally, we see that the precision of the estimated period increases allowing us to reconstruct the phase diagram more reliably. The latter is the result of having many periods of the signal of interest within the observed pass.

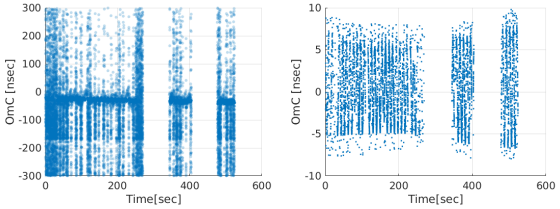

(a)

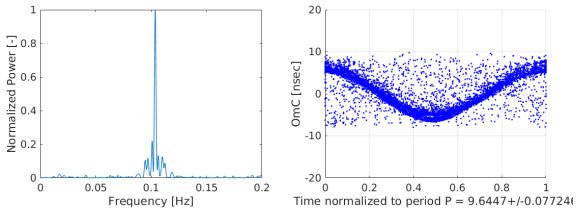

(b)

Figure 8. a) Details of the raw laser ranging residuals (left), and postprocessed signal (right). b) Periodogram (left) and reconstructed phase diagram (right). The pass was observed on January 21, 2022.

5. JASON-2

In this section, we fill focus on the acquired LCs and post-processing challenges for extracting attitude information for Jason-2. We include examples of LCs acquired with the SI1100 on ZIMLAT, and the Andor Neo 5.5 on ZimMAIN. Additionally, we highlight the high temporal resolution achieved by the sCMOS sensor, which enables a better feature characterization if compared to the LCs available acquired with the CCD detector. Furthermore, we analyze the relevance of low-pass filtering selected LCs. To conduct such analysis, we present two examples when the utilization of a low-pass filter on the raw LC improves the estimation of the period. However, we found other cases showing how the application of a low pass filter may lead to the estimation of the wrong period. The presented LCs were acquired on October 9, 2021, and on April 28, 2022.

5.1. CCD vs. sCMOS

In Figure 9 (top) we present a LC acquired with the SI1100 on ZIMLAT, while on Figure 9 (bottom), we show the LC corresponding to observations acquired with the Andor Neo 5.5 on ZimMAIN. Both LCs shown in

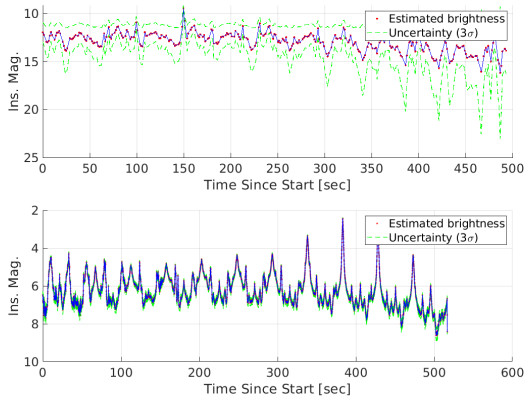

Figure 9. Top: Raw LC observed with the SI1100 on ZIMLAT the 9th of October, 2021. Bottom: Raw LC observed with the Andor Neo 5.5 on ZimMAIN the 28th of April, 2022.

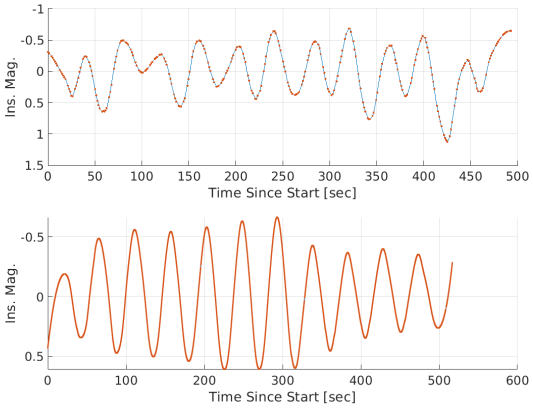

Figure 10. Top: Smoothed LC observed with the SI1100 on ZIMLAT the 9th of October, 2021. Bottom: Smoothed LC observed with the Andor Neo 5.5 on ZimMAIN the 28th of April, 2022.

Figure 9 depict different periodic patterns along the observed pass, and the main detrending of the raw LCs did not yield a significant improvement.
The observations acquired with the SI1100 were taken with an exposure time of 0.2 seconds for the entire pass, while the ones acquired with the Andor Neo 5.5 were exposed 0.1 seconds. Note that for both passes, the acquisition of the measurements included a subframing step. After subframing, the average frame rate achieved with the Andor Neo 5.5 camera was of 10 subframes during one second, while for the SI1100 we acquired on average one subframe per second.

5.2. Filtering of LCs

The first attempt to estimate the synodic period from the top LC in Figure 9 failed. Once again, the issues addressed for the case of LCs from TOPEX/Poseidon was found to be crucial: different patterns along the LC not

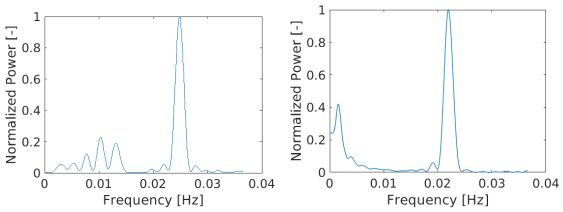

Figure 11. Left: Power spectrum of the observed LC depicted in the top plot in Figure 9. Right: Power spectrum of the observed LC depicted in the bottom plot in Figure 9. The raw top LC depicted in Figure 9 required a smoothing step for being able to estimate the synodic period using the Lomb-Scargle method.

eliminated after the detrending. Moreover, for this particular case, we did not find a solution using the feature-based period estimation algorithm. In this context, we tried to smooth the LC using the robust Box filter, from which the resulting smoothed LCs are presented in Figure 10. After smoothing the LCs, we were able to estimate the synodic period for both passes. For consistency, we estimated the period also for the bottom smoothed LC shown in Figure 10. The conclusion was that the estimated period for the bottom LC in Figure 10 with and without smoothing were in agreement, thus suggesting that there was not a significant loss of information when using smoothed LCs. After the estimation of the synodic period using the Lomb-Scargle method (see Figure 11, we recovered their respective phase diagrams, which are shown in Figure 12.

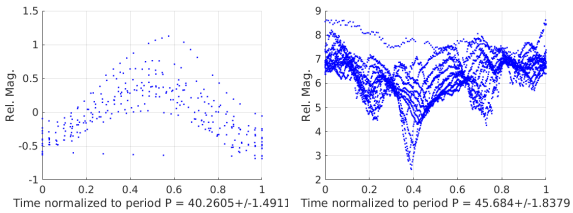

Figure 12. Reconstructed phase diagrams of the different LCs depicted in Figure 9. The left plot shows the phase diagram of the top LC in Figure 9 with required a smoothing step, while the reconstructed phase diagram in the right plot was recovered after removing only the main trend for one of the patterns detected within the complete LC shown at the bottom of Figure 9.

6. ERS-2

The last target object of interest in this work is the defunct satellite ERS-2. The information depicted in this section highlights the benefits of acquiring observations with different observation techniques. Furthermore, the last subsection includes an example of new developments at the SwissOGS highlighting promising results in the spectroscopy of space debris domain.

6.1. Combining Measurements From Different Observation Techniques

We start the analysis by inspection of the simultaneous acquisition of laser ranges and brightness using a passive optical system. From the top LC in Figure 13, we may identify a periodic pattern repeating itself twice until about the second 160. Then, we find an increasing brightness of about 3 magnitudes with respect to the average brightness of the complete pass. However, after the second 160, we also see more dispersion than at the beginning of the pass. This dispersion may not be explained by a low signal-to-noise ratio, since it was indeed high for this portion of the pass. As of the release of this paper, we have not found any reasonable physical explanation for the observed effect, but we were able to confirm the short-period oscillations after the analysis of residuals obtained from the laser ranges from the retroreflector onboard of the defunct satellite (see Figure 14).

After processing the laser ranges, we were able to re-

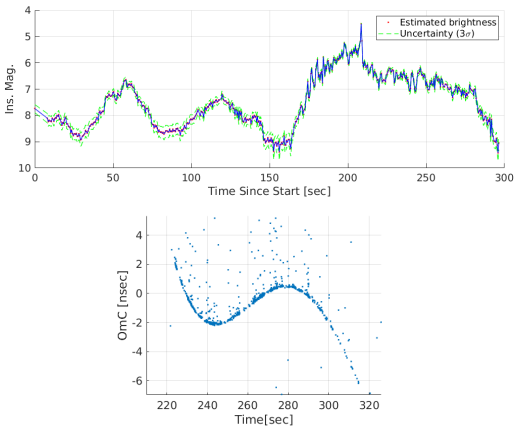

Figure 13. Top: LC acquired with the Andor Neo 5.5. camera on ZIMLAT the 8th of July, 2020. Bottom: resulting residuals after acquiring laser ranges simultaneously with passive optical. Time scales for both plots refer to the beginning epoch of the pass.

trieve one synodic period of the retroflector with respect to the main rotation axis. Note the smooth main signal depicted by the highly concentrated detections in the bottom plot, Figure 13. From the resulting signal, we can see that it complements the LC retrieved with passive optical in the time span when the passive LC became noisier. The combination of the two periodic signals from the LC and laser ranges residuals allowed us to estimate the synodic period, which was found to be of 60 $\pm$ 4 seconds. In a subsequent step, we removed the signal from the laser ranging residuals using a single-pass orbit improvement. The residuals corresponding to the measured ranges suggest that beside the main period depicted in the bottom plot in Figure 13, we have shorter oscillations which could even be correlated with the dispersion that we saw in the passive-optical light curve (see Figure 14). Note that this short oscillations are ideal to be further analyzed with highly-temporal resolution detectors such as sCMOS, photon counters and high repetition rate laser ranging systems. Finally, even though more information

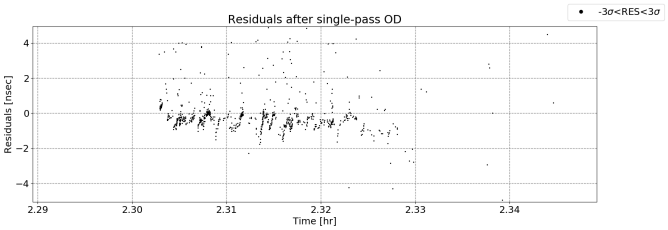

Figure 14. Residuals after a single-pass orbit determination using only laser ranges.

is needed to further confirm our findings, the synergy between the two different techniques show once again the potential to recover more reliably information regarding the attitude state of SD.

Additional LCs were observed for ERS-2 during 2021 using the SI1100 on ZIMLAT. The observed raw LCs are shown in Figure 15. The first LC was observed on February 20. For this LC there was no significant gain after the generic detrending, but the signal-to-noise ratio was relatively low, being mapped one-to-one to larger uncertainties. Additionally, no outstanding feature was identified as being brighter than the average brightness of the observed pass. The estimated synodic period corresponding to this LC was 41.32 $\pm$ 4 seconds. The bottom

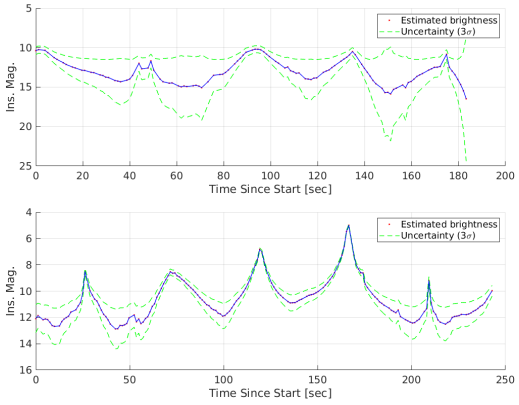

Figure 15. LCs from ERS-2 acquired with the SI1100 on ZIMLAT the 20th of February (top), 2021, and the 23rd of March (bottom), 2021.

LC depicted in Figure 15, which was observed on March 23, showed a significant improvement after removing the main trend, however, as with the previous LC, there was no outstanding bright feature compared to the average brightness of the complete pass. After preprocessing the raw LCs, the estimated synodic period was 45.20 $\pm$ 3 seconds, which is in agreement with the one obtained from the top LC.

6.2. New developments

In this subsection we report on the current developments at the SwissOGS. Since 2021, we started the integration of the Shelyak LISA spectrograph on the second focal station on ZimMAIN. This required an exchange between the Andor Neo 5.5 and the LISA spectrograph, which was done considering the different priorities of the different observation campaigns.
The LISA spectrograph has two CCD detectors in different modules of the instrument. One module has a larger field of view, which is ideal for guiding and target object acquisition. The other module assembles the spectrograph by combining an entrance slit, collimating and imaging optics, grating, and the slit detector. The acquisition of images with LISA is done through a specific version of the software Demetra tailored specifically for the LISA spectrograph. Likewise, the same software is used for postprocessing the raw images.
On June 12, 2022, we were able to observe the defunct satellite ERS-2, in presumably two different attitude states. Before interpreting the results, we will briefly describe the steps that we did to transform the observed spectra in Analog-To-Digital Units (ADU) into normalized reflectance. The data reduction starts by creating *masters* of the bias, darks, flats, and stacking of the object images following the standard practices available for any CCD data reduction scheme. Afterwards, the so-called background is removed and we apply geometric corrections to compensate for distortions effects due to slight misalignment between the different optical imaging elements. To perform the transformation from pixels to wavelengths, we use calibrated emission lines from the Helium-Neon spectral lamp matching those lines with the ones from acquired frames exposed to that source; then, we solve for the coefficients of a degree 4 polynomial, which will allow to perform the radiometric calibration of the raw acquired data. Additionally, one may compensate for the instrument response after fitting the calibrated reflectance spectra of a reference star with the corresponding radiance spectra derived from the raw data.
To derive reflectance spectra, the radiance spectra from the target object is divided by the radiance spectra from a solar analog star type (GV0). The used solar analog to reduce the spectra from ERS-2 was Beta Comae Berenices, which was the nearest from the ones available to the pass of the satellite with respect to the observing station. In Figure 16, we show the acquired frames after data reduction, which were acquired with a gap of 54 seconds in between the acquisition. The retrieved reflectance spectra associated to each frame depicted in Figure 16 are shown in Figure 17.

The signal-to-noise ratio of the top bottom in Figure 17 is worse than for the bottom. Nevertheless, after applying a low pass filter of the obtained reflectance spectra (Lowess), we can identify critical points, steepness, among others to further correlate the resulting spectra with specific materials of the defunct satellite. Furthermore, the top plot in Figure 17 was found to be in agreement with spectra using an independent instrument: the

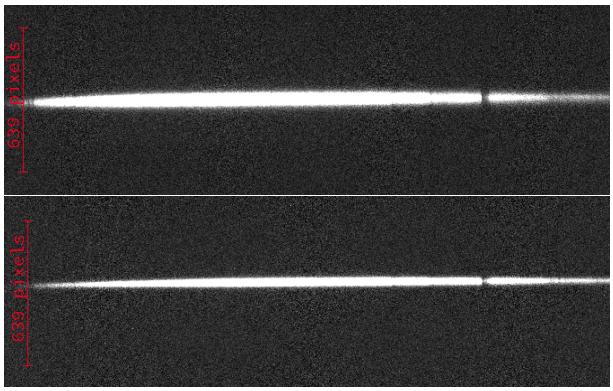

Figure 16. Raw images from ERS-2 corresponding presumably to different poses of the target object with respect to the observing station. The images were acquired with the Shelyak LISA spectrograph mounted on ZimMAIN on June 12, 2022. The top frame corresponds to a less intense glint of the exposed frame compared to the bottom frame. Both frames were acquired with a difference in time of 54 seconds.

so-called All-Sky Meteor Orbit System (AMOS) [6]. For comparison, the results obtained from the AMOS system are shown in Figure 18.

7. SUMMARY

The scope of this work was to provide an update of different targets objects, which are potential good candidates for active debris removal missions. Information regarding the attitude state is crucial for the design of such missions. With that context in mind, we presented observations acquired during the years 2020 and 2022, including attitude related information derived after a substantial improvement of selected systems available at the SwissOGS. The improvements on the different systems include: a) daylight observing capabilities with the Andor Neo 5.5 on ZIMLAT, b) the retrieval of LCs using the Andor Neo 5.5 on ZimMAIN, c) the simultaneous acquisition of observations using active and passive systems for selected targets, and d) the successful retrieval of reflectance spectra using the LISA spectrograph on ZimMAIN. At the processing level we showed particular challenging LCs, from which we could not estimate the synodic period consistently and reliably, highlighting the non-uniqueness of strategies comprising steps from retrieved light curve to the recovery of the synodic period. Per each target object, we included a tailored acquisition and processing strategies to tackle some of the challenges identified during the different acquisition campaigns. Within the new processing strategies, we include the featured-based estimation period, the smoothing of raw LCs, besides the data reduction scheme to reduce data from the LISA spectrograph.

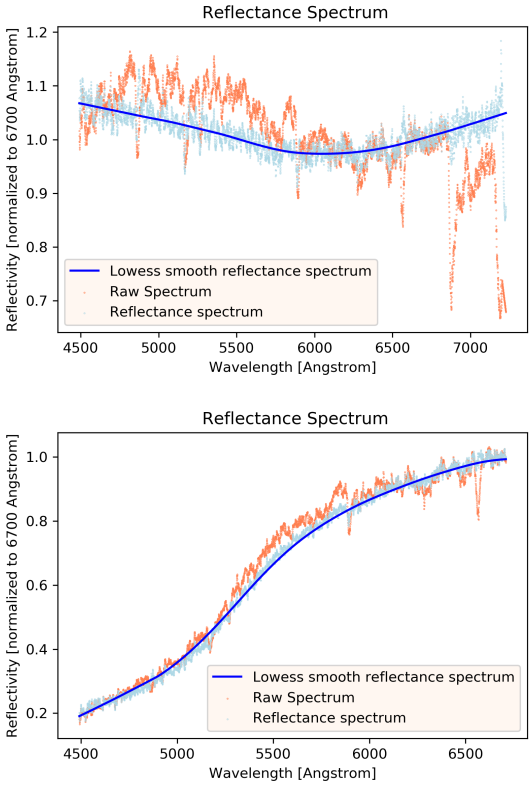

Figure 17. Reflectance spectra of two frames 54 seconds apart of the defunct satellite ERS-2. The bottom plot correlates with similar results from different studies for multi-layer insulation material [5], while the top plot might come from the radio antenna onboard the defunct satellite.

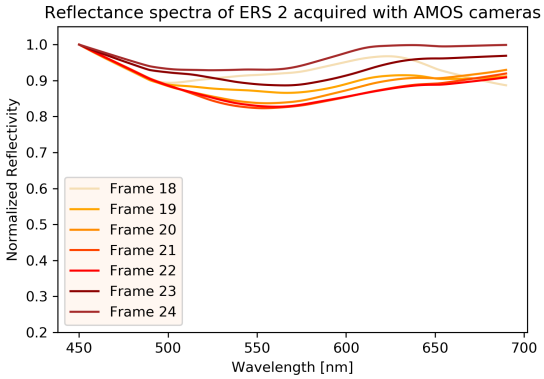

Figure 18. Reflectance spectra of two the defunct satellite ERS-2 using the AMOS observing system during the glinting phase [6].

REFERENCES

1. European Space Agency (2022). ESA Strategy towards Zero Debris – the Evolution of Spacecraft Platforms. Webinar.
2. Shan, M. (2018). Net deployment and contact dynamics of capturing space debris objects. Doctoral Dissertation, Delft University of Technology.
3. Rachman, A., Schildknecht, T., Silha, J., Pittet, J. N., & Vananti, A. (2017, September). Attitude state evolution of space debris determined from optical light curve observations. In Proceedings of 68th International Astronautical Congress (IAC), Adelaide, Australia (pp. 25-29).
4. Rodriguez-Villamizar, J., & Schildknecht, T. (2022). Daylight Measurement Acquisition of Defunct Resident Space Objects Combining Active and Passive Electro-Optical Systems. IEEE Transactions on Geoscience and Remote Sensing, 60, 1-17.
5. Rodriguez, H. M., Abercromby, K. J., & Barker, E. (2007). Optical properties of multi-layered insulation. In Advanced Maui Optical and Space Surveillance Technologies (AMOS) Conference, Maui (HI), USA.
6. Zilkova, D., Silha, J., Matlovic, P. et al. (2022). Space debris spectroscopy: specular reflections at leo regime. Advances in Space Research. doi:https://doi.org/10.1016/j.asr.2022.12.001.
7. Africano, J., Kervin, P., Hall, D., Sydney, P., Ross, J., Payne, T., Gregory, S., Jorgensen, K., Jarvis, K., Parr-Thumm, T., Stansbery G., & Barker, E. (2005). Understanding photometric phase angle corrections. In Proceedings of the 4th European Conference on Space Debris (Vol. 587, pp. 141-146).
8. Linder, E., Silha, J., Schildknecht, T., & Hager, M. (2015). Extraction of spin periods of space debris from optical light curves. In Proceedings 66th International Astronautical Congress 2015 (IAC 2015).
9. Pittet, J. N., Silha, J., & Schildknecht, T. (2018). Spin motion determination of the Envisat satellite through laser ranging measurements from a single pass measured by a single station. Advances in space research, 61(4), 1121-1131.